# Supplemental Information for:

## Rivers in reverse: upstream-migrating dechannelization and flooding cause avulsion on fluvial fans

*Douglas A. Edmonds[1], Harrison K. Martin[1], Jeff Valenza[1], Riley Henson[1], Gary S. Weissmann[2], Keely Miltenberger[2], Wade Mans[2], Jason R. Moore[3], Rudy Slingerland[4], Martin Gibling[5], Alexander B. Bryk[6], and Elizabeth Hajek[4]*

[1]*Indiana University, Department of Earth and Atmospheric Sciences, 1001 E. 10th St, Bloomington, Indiana, 47405-1405*

[2]*University of New Mexico, Department of Earth and Planetary Sciences, MSC 03 2040, 1 University of New Mexico, Albuquerque, NM 87131-0001*

[3]*University of New Mexico, Honors College, MSC 06 3890, 1 University of New Mexico, Albuquerque, NM 87131-0001*

[4]*Penn State University, Department of Geosciences, 423 Deike Bldg., University Park, PA 16802*

[5]*Dalhousie University, Department of Earth and Environmental Sciences, 1459 Oxford St., P.O. Box 15000, Halifax, Nova Scotia, Canada B3H 4R2*

[6]*The University of California Department of Earth and Planetary Science, 307 McCone Hall, University of California, Berkeley, CA 94720-4767*

Contents:

## 1. Finding Retrogradational Avulsions

We searched throughout the Andean and Papuan foreland sedimentary basins. The Andean and New Guinean sedimentary basins are actively accumulating sediment from rivers draining their respective mountain belts. When these river transition to the lower-slope foreland basin they rapidly aggrade their bed and frequently avulse, which creates megafans in the proximals parts of the Andean and New Guinean basins (Horton and DeCelles, 2001; Weissmann et al., 2010, 2015; DeCelles, 2011). In between the large megafans are smaller interfans (Weissmann et al., 2015), where we commonly find these retrogradational avulsions. We could not automate our search, but having multiple researchers search through each area multiple times, we are confident that we found all the obvious retrogradational avulsions. We used the presence of the upstream-migrating chevron of dead trees to identify these avulsions.

We searched for retrogradational avulsions in Landsat data using Google Earth Engine, a cloud-computing platform for analysis of remote sensing data (Gorelick et al., 2017). We use only Landsat data because it has a native resolution of 30 m per pixel, which is just fine enough to detect most of these avulsions, and Landsat has nearly global coverage from 1984 and 2018. Many of the retrogradational avulsions are directly observable in the Google Earth Engine Timelapse (https://earthengine.google.com/timelapse/), but in other cases it can be difficult to identify the characteristic upstream-migrating chevron because of clouds or poor image quality. In those instances, we used the Google Earth Engine application programmable interface to build monthly to yearly composite images from Landsat data. Each composite image was created by chronologically ordering all Landsat scenes from a given year, and then reducing that three-dimensional matrix into two dimensions by selecting, on a pixel-by-pixel basis, the most recent, cloud-free value for each pixel position.  This creates a single time-transgressive composite image for each year. We transformed each composite image into different indices sensitive to water and vegetation to find additional evidence of the upstream-migrating chevron. In cases where the upstream-migrating chevron was small and hard to identify even using Landsat data, we used high-resolution Maxar imagery if it was available.

## 2. Description of data in Table S1 (table provided in the supplement)

### a. Start and End Year and Location

Start and end year were identified in Google Earth Engine as the year with the first clear sign of an upstream-migrating chevron. For cases where the start year is 1984 or the end year is 2018, we did not observe the initiation or ending of the avulsion. In those cases, any calculated duration may not represent the true lifespan of the avulsion. We marked the starting and ending position at the tip of the upstream-migrating chevron at the starting and ending years and recorded their latitude and longitude in the starting/ending latitude/longitude columns.

### b. Ongoing at start or end

If the avulsion was already in progress in the first useable composite image then it was marked as ongoing at the 'start'. If the avulsion was not completed by the last year it was marked as ongoing at the 'end'. If the avulsion was ongoing at the start and end it was marked 'both'.

### c. Dechannelization distance and velocity

We measure the dechannelization distance by tracing the channel centerline from the starting to ending point of the retrogradational avulsion. We trace these centerlines in ArcGIS using either Landsat Imagery from at least the start and end of the avulsion or Google Earth where the resolution is good enough to see the channel. We measure the rate by taking the distance of the centerline divided by the duration (calculated as end year minus start year). In cases where imagery resolution is not sufficient, we use high-resolution data from Maxar, which consists of imagery from WorldView 1 through 4, QuickBird, and GeoEye, when available. Given the incomplete coverage of Maxar imagery, we could not find high-resolution images for each avulsion. These images are available from ~2003 to present and usually have sub-meter pixel resolution. All centerlines from retrograding channels are available as supplemental data associated with this paper.

*d. Drainage basin area and river discharge*

We use the RiverATLAS (Linke et al., 2019) to extract drainage basin area and discharge. RiverATLAS provides global hydrography for river networks at a 15 arc-second (~500 m) resolution. Attributes for the river networks are provided at sub-basin scale and are separated by river link. We extracted drainage basin area and the maximum yearly discharge from the river link closest to the starting location of each retrogradational avulsion. We deviated from this rule if there were major tributaries just downstream of the starting location, in which case our extraction point was moved to those locations. For a few cases, the repositioning of the river during the retrogradational avulsions caused a mismatch between the extracted network and the present position of the river. In those cases, we selected the extraction position based on the initial position of the river.

For each river link that coincided with the position of the avulsion we extracted the maximum yearly discharge. Maximum yearly discharge is derived from long-term (1961–90) monthly discharge averages calculated by the WaterGAP model (Döll et al., 2003). WaterGAP uses inputs of precipitation and other relevant climatic variables to calculate a water balance that accounts for sources and sinks. The outflow of water from any given cell is assumed to be through a river segment. The outflow of water, or river discharge, is calculated at 0.5° resolution and every month. Lehner and Grill (2013) downscaled the WaterGAP discharge to 15 arc-second resolution. Importantly, the underlying simulation of runoff generation is still the WaterGAP model performed at 0.5° resolution. The results are geospatially downscaled to fit the 15 arc-second grid in RiverATLAS. The downscaled discharges are measured to 0.001 $m^3$/s, but accuracy at that level is not entirely reliable. Linke et al. (2019) validated the downscaled discharge data and found for flows ranging from 0.004 to 180,000 $m^3$ $s^{-1}$ ($n$ = 3,003) that there was a strong correlation between modeled and observed data ($R^2$ = 0.99). For our characterization of discharge, we selected the yearly maximum discharge because it is likely representative of the high flow conditions that drive sedimentation and migration of retrogradational avulsions.

*e. River Width*

Most of the retrogradational avulsions occur on narrow rivers, and widths were measured from imagery with sub-meter pixel resolution from Maxar or meter resolution from Planet. We measured width upstream of the ending point of the retrogradational avulsion at 5-8 different channel-centerline-perpendicular cross sections that were unaffected by the avulsion and its far-field effects. Where possible, we made measurements in Google Earth, but also

used high-resolution satellite data from Maxar. The sources of data for each width measurement are listed in Table DR1. For rivers with multiple retrogradational avulsions we calculated an average width for all measurements from all avulsions and assigned that to each sample from the same river.

### f. Slope

We measured the topographic slope along each centerline from starting to ending location on each retrogradational avulsion. We extracted the elevation from Shuttle Radar Topography Mission (SRTM) 30-m data for points along the centerline. The slope was calculated from the best-fit ordinary least squares linear regression. When retrogradational avulsions were short, we had to extend the centerlines to provide sufficient drop in topography for the slope calculation. In these cases, we preferentially extended the centerlines upstream for the slope measurements since the channel downstream was not visible due to dechannelization. Not all slopes could be calculated with the SRTM data given the noise and the vertical resolution. In those cases, we used the terrain layer in Google Earth to find a baseline long enough to define a slope. For rivers with multiple retrogradational avulsions, we assign them all the same slope if the elevations were not statistically distinct.

## 3. Additional examples of retrogradational avulsions

### a. Slope break data for R3.1 and R3.2
To evaluate what initiated the avulsions we investigated whether they begin at slope breaks on the fluvial fans (Figure S1). To estimate the slope we extracted satellite-derived bare-earth elevation data from the ICESat-2 mission (openaltimetry.org). ICESat-2 is a space-based laser altimetry mission launched by NASA in 2018. We used data product ATL08, which provides accurate bare-earth elevation and vegetation canopy height values (Wang et al., 2019). A description of how bare-earth elevations are determined is available in Neuenschwander and Pitts (2019).

ICESat-2 elevation profile shows no obvious break in slope associated with avulsions R3.1 and R3.2 (top panel, Figure S1). A 30 m moving window slope calculation confirms that there is not an obvious slope break associated with the beginning of each avulsion (top panel, Figure S1). If dechannelization were associated with significant slope change, we would expect to find the avulsion positioned at the edge of the fan where slopes abruptly change. But the positions of R3.1 and R3.2 are not clearly on the edge of the fan, though R3.2 is much closer. Additionally, other avulsions in the area are shown and they are away from the fan edge. Note that these ICESat-2 slope data were not used to determine the slope in Table S1.
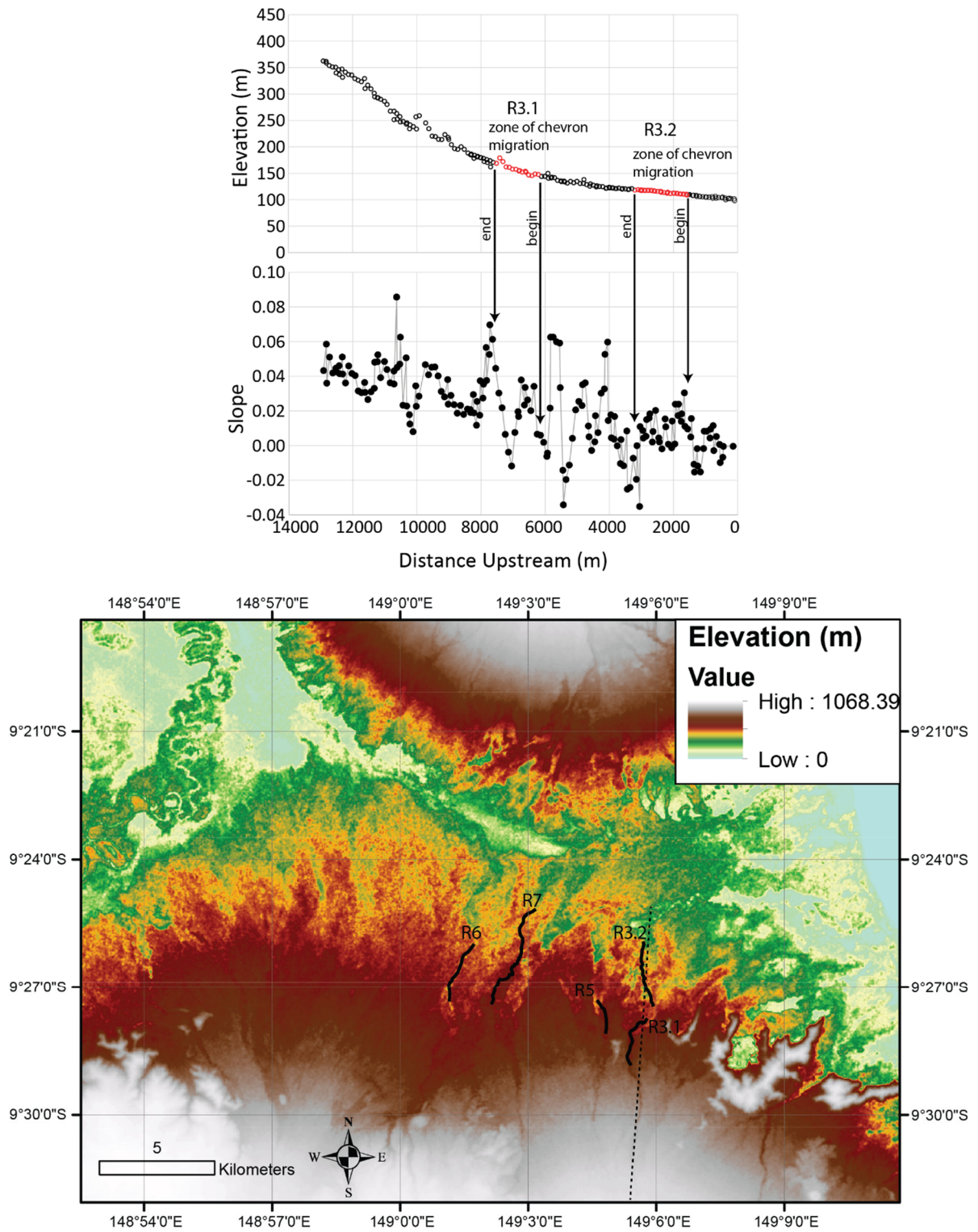
*Figure S1: Changes in slope are not clearly associated with retrogradational avulsions in Papua New Guinea. Top panel: ICESat-2 bare-earth elevations along dotted line track in bottom figure. Zone of chevron migration is shown in red and on the map in black. Immediately below is a 30 m moving window slope value shows no obvious slope reduction where the chevron begins migrating. Lower panel: 30 m shuttle radar topography mission digital elevation model showing the positions of the avulsions in this area.*
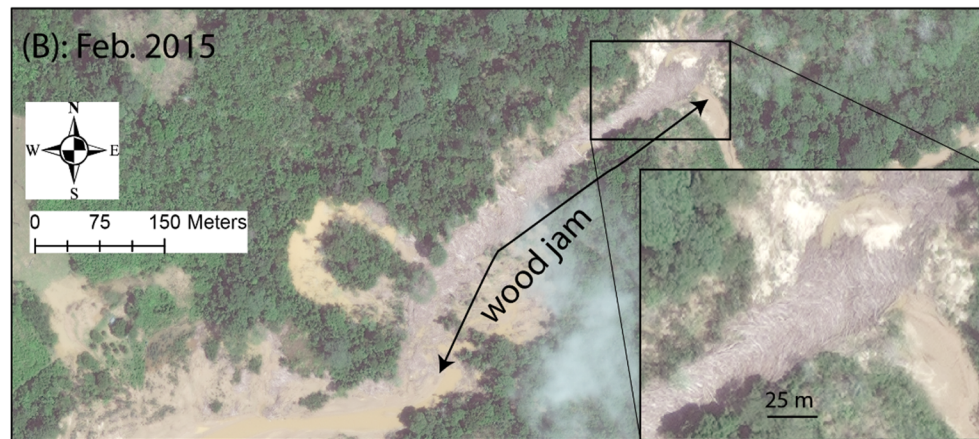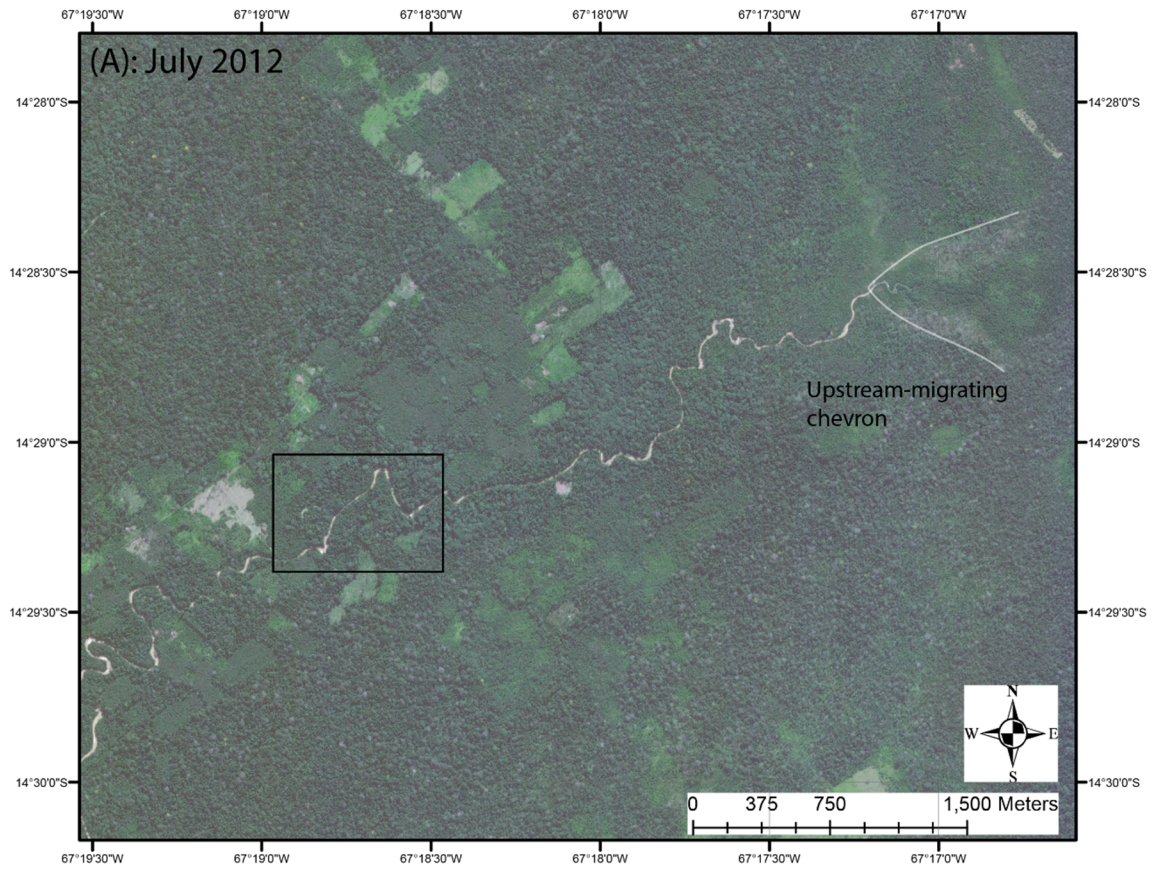
*b.* *Woody Debris*





Figure S2: Avulsion R19.3. (A) Overview of the avulsion when it first started forming in 2012. (B) After the avulsion migrated upstream from its initiation point in (A) to its current position in (B) there is large accumulation of woody debris (identified by eye, see inset) where the channel goes from water to filled with sediment. Images are from WorldView, Imagery Copyright 2021 Maxar, Inc.

In all of our examples we cannot clearly define what initiates the upstream-migrating waves of dechannelization. We have only found retrogradational avulsions on heavily forested fans,

and we often see large accumulations of woody debris during the dechannelization process (Figure S2). Therefore, we expect that woody debris in the form of logjams are an important contributor to channel blockage. Log jams were observed by Lombardo (2017) on rivers in Bolivia.

## 4. Model Description

Consider a straight river reach at bankfull flow with a slope $S$ [ - ], a wetted cross-sectional area $A$ [m$^2$], and a blockage of height $b_h$ [m] in the middle of the channel that spans the channel width (Figure S3). At the upstream boundary a steady uniform water discharge $Q_{in}$ [m$^3$ s$^{-1}$] comes into the domain. The water velocity $V$ [m s$^{-1}$] in the domain will be non-uniform as the depth $h$ changes in response to the blockage. This will create a rise in water surface elevation some distance upstream of the blockage, similar to a backwater effect. Because the channel is at bankfull flow stage, the rise in water surface will create overbank flow ($q_n$ [m$^2$ s$^{-1}$]) on both sides of the channel over some length $L$ that scales with the backwater (inset Figure S3). The overbank flow will reduce the discharge and water depth downstream of the blockage in the main channel, possibly drying out the channel, and it will also decelerate flow and reduce bed shear stress upstream of the blockage due to the backwater effect. These two factors, in some cases, should cause the channel to deposit sediment and aggrade its bed upstream of the blockage, or in other cases the acceleration of flow on the downstream side of the blockage should be enough to erode the blockage and return the channel to a flat-bed configuration. The model is built to explore these situations and determine what conditions lead to runaway upstream migration of the blockage (infilling wedge) due to sediment deposition.
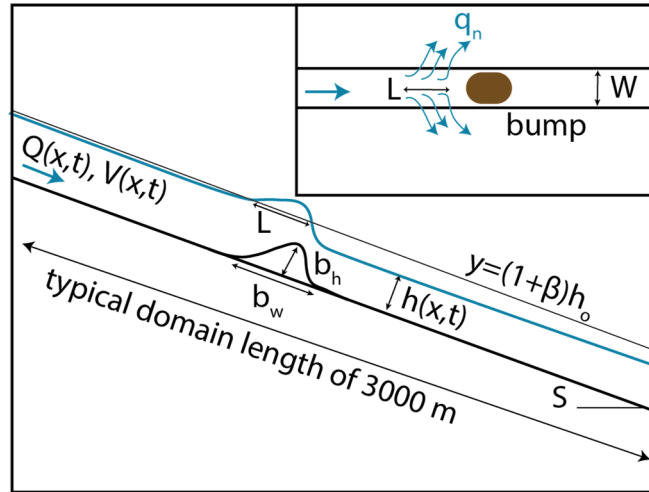


*Figure S1: Model Definition Sketch showing a river profile along the centerline. Inset figure shows sketch of the planview.*

### a. Governing Equations

Under these conditions, the time evolution ($t$) of the flow field can be given by the nonuniform St. Venant's Equations for conservation of mass (eq 1) and momentum (eqs 2 and 3) of fluid discharge in a river channel.

$$\frac{\partial A}{\partial t} + \frac{\partial Q}{\partial x} - q_n = 0 \quad (1)$$

$$\frac{\partial Q}{\partial t} + \frac{\partial (QV)}{\partial x} + gA\left(\frac{\partial h}{\partial x} - S + S_f\right) = 0 \qquad (2)$$

$$S_f = \frac{f}{8gh}\frac{|Q|Q}{A^2} \qquad (3)$$

Where $x$ is the distance along the channel centerline [m], $A$ is cross-sectional channel area [m$^2$], and $g$ is acceleration due to gravity [m$^2$ s$^{-1}$]. $S_f$ is the friction slope, which depends on the Darcy-Weisbach friction factor $f$.

The evolution of the bed is given by the Exner equation

$$\frac{\partial \eta}{\partial t} = -m_{sf} * \frac{1}{1-\lambda_p}\frac{\partial q_s}{\partial x} \qquad (4)$$

Where $\eta$ is bed elevation [m], and $\lambda_p$ is sediment porosity [ - ], and $m_{sf}$ is a morphological scale factor [ - ] that is meant to accelerate bed elevation change. The transport rate of the bed material load $q_s$ [m$^2$ s$^{-1}$] is given by

$$q_s = 8\sqrt{RgD^3}(\tau^* - \tau_c^*)^{\frac{3}{2}} \qquad (5)$$

where $R = (\rho_s - \rho)/\rho$, $\rho_s$ is the sediment density (assumed to be 2650 kg m$^{-3}$) and $\rho$ is the water density (1000 kg m$^{-3}$), $D$ is the particle diameter [m], $\tau^* = \frac{\tau_b}{(\rho_s-\rho)gD}$ is the Shields number ($\tau_c^*$ is the value at the threshold of motion), and $\tau_b = \frac{\rho*f*V^2}{8}$. For simplicity, we assume that the bed consists of a single grain size. We have little field data that suggests what this grain size should be, so we use 3 mm for all model runs. Sensitivity tests show that results are generally insensitive to grain size.

We also need a relation that describes the volume of overbank flow $q_n$ that occurs in response to water flowing over the blockage. There is not an obvious choice for how to formulate $q_n$. It should depend on the height of the water above the levees, the flow conditions in the channel, and the bed surface slope away from the channel at the point of overbank flow. We choose to use quasi-theoretical relationships that describe flow through a side weir (also called lateral weir) in a channel (Hager, 1987; Emiroglu et al., 2011). A side weir is a notched portion of the channel that has a lower elevation than the banks up and downstream. This notched portion allows flow to escape. An equation describing the volume of flow leaving the notch of length $L$ and height $y$ above the bed was derived by de Marchi (1934) as

$$q_n = L * \frac{2}{3}C_d\sqrt{2g}(h - y)^{\frac{3}{2}} \qquad (6)$$

Where $C_d$ is an empirically derived coefficient of discharge determined from experimentation. Ranga Raju et al., (1979) determined that $C_d = 0.81 - 0.6 * F_o$, where $F_o$ is the Froude number of the upstream flow that is unaffected by the side weir and is given as $F_o = \frac{V_o}{\sqrt{g*h_o}}$ where the subscript "$o$" refers to equilibrium values of variables calculated at the boundary well upstream of the blockage. This is conveniently calculated from the normal flow relation

$$h_o = \left(\frac{f*Q_{in}^2}{8*g*S_o*W^2}\right)^{\frac{1}{3}} \qquad (7)$$

8

In our implementation of equation (6) we set $y = (1 + \beta)h_o$. This effectively means that overbank flow only occurs where $h > (1 + \beta)h_o$ and we set $L$ as this distance over where overbank flow occurs. We use $\beta = 0.05$. We tested other values and found the results did not change substantively.

### b. Simplifying Assumptions

In this model, we assume accelerations over the blockage are gradual enough that pressure does not deviate from hydrostatic and can be described by 1D flow. Also, we assume there are no input or outputs of water except for $q_n$, which is reasonable over the short domain lengths. We handle overbank flow in the model by assuming it does not return to the channel, which is consistent with all observations of the areas covered by the avulsion. We also use a side-weir formulation to calculate the overbank flow because it is physically motivated and it is related to the conditions in the channel. But the side weir formulation describes flow that would be free-falling over the side weir, which does not occur in natural river systems. We assume that the channel cross-sectional area can be approximated by a rectangle and that the width $W$ [m] does not change in time or space.

### c. Initial and Boundary conditions

At the upstream boundary of the model, we specified a steady, incoming discharge and a sediment concentration that is in equilibrium with the flow so that no bed level changes occur. At the downstream boundary we specify a zero-gradient water surface elevation boundary condition where the elevation of the boundary node is always equal to the node just upstream. This allows the water surface to smoothly exit the domain and fluctuate up or down in response to changes in flow volume.

The initial condition is an equilibrium bed-surface slope that depends on discharge and width calculated via equation (7). Once that slope was determined, we placed a Gaussian blockage in the middle of the channel.

### d. Solving the model

To calculate flow over the blockage and the associated bed level changes, we solved equations 1 and 2 with a linearized four-point implicit scheme (Slingerland and Kump, 2011). Equation 4 was solved using a blended upwind and downwind explicit finite difference scheme.

We first allowed the model to reach steady state without any overbank flow or any changes in bed level defined by a conservation of mass tolerance where every node had the same discharge to within 0.01% of the incoming flow. Once steady state was achieved, we initiated the overbank flow routine and used equation 6 to determine the amount of overbank flow. If the blockage forced enough water out of the channel, then nodes could become dry. We used a wetting and drying threshold following the thin film approach (Medeiros and Hagen, 2013) where we assumed any cell with $h < 0.05$ m is considered dry. To avoid numerical instabilities, we assume that all cells downstream of a dry cell are also instantaneously dried. Once the overbank flow routine was initiated, it usually took about 2 hours of model time to reach a new equilibrium. After that new equilibrium was achieved, we allowed the bed level to change and the model to evolve. We assume that the channel heals itself if the blockage reduces to height less than 1/5 of the initial blockage height. We assumed the channel is

dechannelizing if it migrated upstream from its initial position for 10 model nodes (nominally 300 m) because the model does not incorporate selecting a new flowpath.

## 5. Model experiments and parameters

We conducted 648 model runs across different values of $S$, $Q_{in}$, $W$, and $b^*$ (Table S2). Other model parameters are listed in this table, as well. Each model experiment consisted of a unique combination of $S$, $Q_{in}$, $W$, and $b^*$ and each experiment was run until the blockage eroded to 20% of the initial height (categorized as 'healing') or dechannelized for 10 model nodes (categorized as 'dechannelizing').

| Variable | Units | Value used (brackets denote values used across a given parameter) |
|---|---|---|
| $Q_{in}$ | $m^3\ s^{-1}$ | [2, 4.1, 8.7, 18.3, 38.2, 79.9] |
| $S_o$ | n/a | [0.0002, 0.00039, 0.00077, 0.0015, 0.0029, 0.0056] |
| $W$ | m | [10, 25, 40] |
| $b* = b_h/h_o$ | n/a | [0.5, 0.6, 0.7, 0.8, 0.9, 1] |
| $\beta$ | n/a | 0.05 |
| $D$ | M | 0.003 |
| $dt$ | S | 1 |
| $dx$ | M | 10 |
| $\rho_s$ | $kg\ m^{-3}$ | 2650 |
| $\rho$ | $kg\ m^{-3}$ | 1000 |
| $f$ | n/a | 0.15 |
| $\tau_c^*$ | n/a | 0 |
| $m_{sf}$ | n/a | 30 |
| $\lambda_p$ | n/a | 0.3 |

Table S2: Model Parameters used in this study

### a. Zone of overbank flow

When water flows over the blockage the water surface rises in elevation and that rise extends upstream for some distance $L$ (see schematic inset in Fig. S3 and example model output in Fig. S4). This backwater effect is a key mechanism that drives the dechannelization process. An example of the backwater effect for different blockage heights is shown in Figure S4. The zone of overbank flow associated with these blockages would extend from about 1350 m to 1500 m.
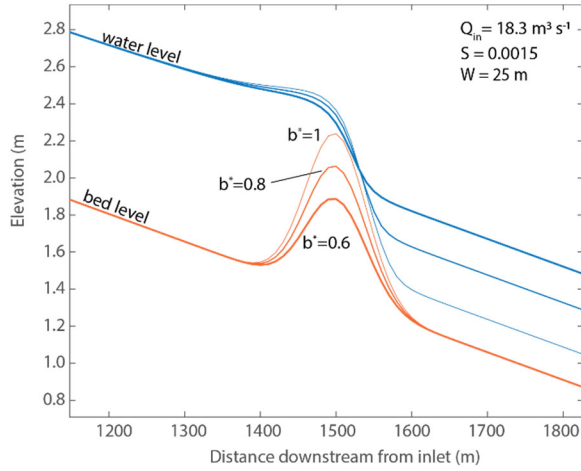
*Figure S2: Water surface elevation changes due to the presence of a blockage. The blockage causes the water surface elevation upstream to rise, and that rise extends upstream, in this example 100 to 150 m. This backwater zone then creates overbank flow because of the elevated water surface. The backwater increases in height and length as the size of the blockage increases. $b^*$ is the blockage height divided by the normal flow depth. Normal flow depth is given in eq. 7.*

## b. Effect of Channel width

Channel width had a minimal effect on the tendency for dechannelization. The threshold line for dechannelization moves to the upper left for narrower channels and the lower right for wider channels. The effect of increasing the width from 10 m to 40 m only slightly changed the position of the threshold line (Figure S5).
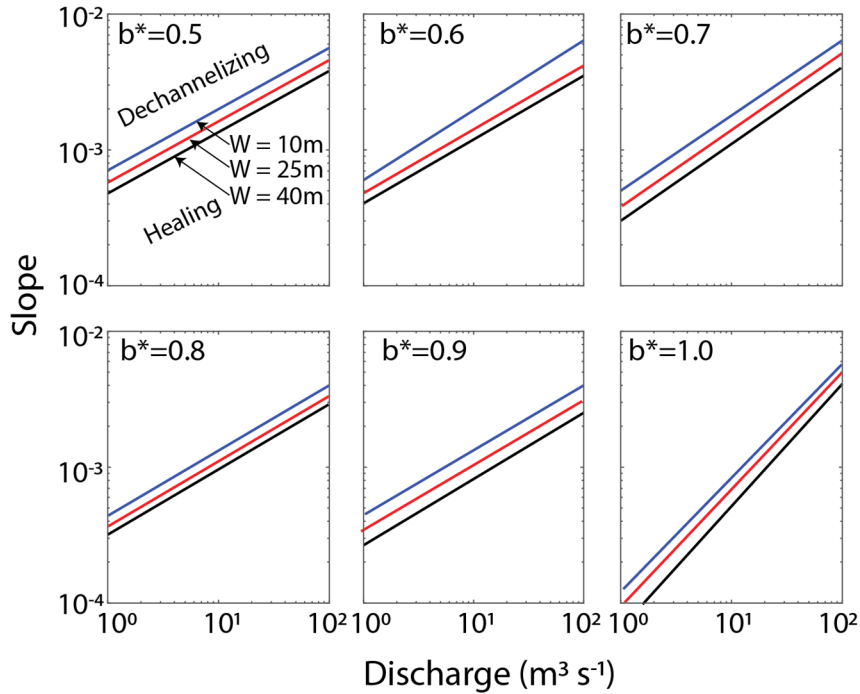


*Figure S3: Effect of width on dechannelization. Model runs were calculated for evenly spaced values of discharge and slope across the parameter space shown. Each run was classified as dechannelizing or healing (See section 5 for more details). The solid lines represent the threshold discharge-slope value for dechannelization.*

# REFERENCES

De Marchi, G., 1934, Essay on the performance of lateral weirs: L'Energia Elettrica, Milan, Italy, v. 11, p. 849–860.

DeCelles, P.G., 2011, Foreland basin systems revisited: Variations in response to tectonic settings: Tectonics of Sedimentary Basins: Recent Advances: New York, John Wiley & Sons, p. 405–426.

Döll, P., Kaspar, F., and Lehner, B., 2003, A global hydrological model for deriving water availability indicators: model tuning and validation: Journal of Hydrology, v. 270, p. 105–134, doi:10.1016/S0022-1694(02)00283-4.

Emiroglu, M.E., Agaccioglu, H., and Kaya, N., 2011, Discharging capacity of rectangular side weirs in straight open channels: Flow Measurement and Instrumentation, v. 22, p. 319–330, doi:10.1016/j.flowmeasinst.2011.04.003.

Gorelick, N., Hancher, M., Dixon, M., Ilyushchenko, S., Thau, D., and Moore, R., 2017, Google Earth Engine: Planetary-scale geospatial analysis for everyone: Remote Sensing of Environment, v. 202, p. 18–27.

Hager, W.H., 1987, Lateral Outflow Over Side Weirs: Journal of Hydraulic Engineering, v. 113, p. 491–504, doi:10.1061/(ASCE)0733-9429(1987)113:4(491).

Horton, B., and DeCelles, P., 2001, Modern and ancient fluvial megafans in the foreland basin system of the central Andes, southern Bolivia: Implications for drainage network evolution in fold-thrust belts: Basin research, v. 13, p. 43–63.

Lehner, B., and Grill, G., 2013, Global river hydrography and network routing: baseline data and new approaches to study the world's large river systems: Hydrological Processes, v. 27, p. 2171–2186, doi:https://doi.org/10.1002/hyp.9740.

Linke, S. et al., 2019, Global hydro-environmental sub-basin and river reach characteristics at high spatial resolution: Scientific Data, v. 6, p. 283, doi:10.1038/s41597-019-0300-6.

Medeiros, S.C., and Hagen, S.C., 2013, Review of wetting and drying algorithms for numerical tidal flow models: International Journal for Numerical Methods in Fluids, v. 71, p. 473–487, doi:https://doi.org/10.1002/fld.3668.

Neuenschwander, A., and Pitts, K., 2019, The ATL08 land and vegetation product for the ICESat-2 Mission: Remote Sensing of Environment, v. 221, p. 247–259, doi:10.1016/j.rse.2018.11.005.

Ranga Raju, K.G., Gupta, S.K., and Prasad, B., 1979, Side Weir in Rectangular Channel: Journal of the Hydraulics Division, v. 105, p. 547–554, doi:10.1061/JYCEAJ.0005207.

Slingerland, R., and Kump, L., 2011, Mathematical Modeling of Earth's Dynamical Systems: A Primer: Princeton University Press.

Wang, C. et al., 2019, Ground elevation accuracy verification of ICESat-2 data: a case study in Alaska, USA: Optics Express, v. 27, p. 38168–38179, doi:10.1364/OE.27.038168.

Weissmann, G.S., Hartley, A.J., Nichols, G., Scuderi, L.A., Olson, M., Buehler, H., and Banteah, R., 2010, Fluvial form in modern continental sedimentary systems: Distributive fluvial systems: Geology, v. 38, p. 39–42.

Weissmann, G., Hartley, A., Scuderi, L., Nichols, G., Owen, A., Wright, S., Felicia, A., Holland, F., and Anaya, F., 2015, Fluvial geomorphic elements in modern sedimentary basins and their potential preservation in the rock record: A review: Geomorphology, v. 250, p. 187–219.